

Amorphization of Ge and Si nanocrystals embedded in amorphous SiO₂ by ion irradiationM. Backman,¹ F. Djurabekova,^{1,2,*} O. H. Pakarinen,¹ K. Nordlund,¹ L. L. Araujo,³ and M. C. Ridgway³¹*Helsinki Institute of Physics and Department of Physics, University of Helsinki, P.O. Box 43, Helsinki FI-00014, Finland*²*Arifov Institute of Electronics, Durmon yuli 33, 100125 Tashkent, Uzbekistan*³*Department of Electronic Materials Engineering, Research School of Physical Sciences and Engineering, Australian National University, Canberra, Australian Capital Territory 0200, Australia*

(Received 31 July 2009; revised manuscript received 18 September 2009; published 19 October 2009)

Finite-size effects become significant in nanoscale materials. When a nanocrystal is surrounded by a host matrix of a different nature, the perfection of the crystal structure is distorted by the interface formed between the nanocrystal and the matrix. The larger the surface-to-volume ratio of the nanocrystal, the higher the influence of the interface defect states on its properties. The presence of defect states in the interface can also explain the different responses of the nanocrystals (NCs) on external influences. By the combination of molecular-dynamics simulations and x-ray absorption spectroscopy measurements, we show that the amorphization of Si and Ge nanocrystals is reached at doses roughly one order of magnitude lower than those for the bulk crystals. Examining nanocrystals in the size range from 2.4 to 9 nm, we also show that the susceptibility to the amorphization decreases with increasing nanocrystal size. The finite-size effect remains significant also for the largest nanocrystals of 9 nm.

DOI: [10.1103/PhysRevB.80.144109](https://doi.org/10.1103/PhysRevB.80.144109)

PACS number(s): 61.82.Rx, 61.80.Lj, 79.20.Rf, 81.07.Ta

I. INTRODUCTION

The size range of nanocrystals (NCs) encompasses crystals starting from a few tens of atoms to a few tens of nanometer size, which, thanks to recent progress in nanoscience and technology, find various applications in industry and daily life. In this scale, the surface-to-volume ratio is not negligible anymore originating from the so-called finite-size effects. Using this ratio one can ascribe certain behavior and properties to nanocrystals, providing a way to increase controllability of nanostructures. Nevertheless, it is not yet clear what effect the size, being limited to a few lattice parameters, has on the properties and consequent behavior of a crystal under external influences.

An embedded nanocrystal is confined within a matrix; in such a system the finite-size effect is even more profound, since the nanocrystal faces not vacuum but another material with different structural properties. In this case, the structural mismatch of both materials will strongly affect the interface between them. In its turn, the interface will spread the strain field deeper into both materials. If the matrix is amorphous, such as amorphous silica (*a*-SiO₂) (conventionally used in the Si-based microelectronic industry and as the host material for Si and Ge nanocrystals), the different ordering of atoms in both structures makes this effect more profound. Thus, the properties of an embedded nanocrystal might experience stronger influence of the interface.

It has already been shown by many researchers that the nanostructures indeed exhibit properties distinctly different from those of the same material in the bulk. For instance, nanocrystals can melt at a temperature higher or lower than their bulk counterparts.¹⁻³ The ionization energy, electron affinity,⁴ and photoluminescence lifetime⁵ for elemental semiconductor nanocrystals can not only be different from bulk but can also be strongly size dependent.

As one of the key processes for the fabrication of embedded nanocrystal structures, ion-beam irradiation requires a

proper analysis of its consequences on an irradiated material. It can also be successfully applied as a way of tuning the material's properties. For instance, in some cases the size and spatial distribution of the nanocrystals can be controlled by high-energy ion irradiation of the preformed embedded nanocrystals.⁶ On the other hand, the photoluminescence of Si NC/(*a*-SiO₂) was found to respond noticeably to the number and nature of defect sites created in the structure during ion irradiation.^{7,8} However, as far as the crystal structure is concerned, the modification of embedded NCs is limited by the amorphization of the crystals as defects begin to predominate in their structures. A recent surprising experimental observation was that metal nanocrystals confined in *a*-SiO₂ were found to be rendered amorphous during ion irradiation.⁹ There is also previous indirect evidence from photoluminescence measurements that Si nanocrystals are easier to amorphize than bulk Si.¹⁰

In this work, by a combination of molecular-dynamics (MD) simulations and extended x-ray absorption spectroscopy (XAS) measurements, we show that Si NCs and Ge NCs embedded in *a*-SiO₂ can be rendered amorphous by ion irradiation doses considerably lower than those needed to amorphize the bulk counterparts. We also discuss the possible mechanism responsible for the amorphization. As a result of the effect of the surface-to-volume ratio, the amorphization dose of the NCs is found to depend on the diameter of the NCs. The larger the ratio (the smaller the NC diameter), the lower is the dose required to initiate the amorphization process.

II. METHODS**A. Experiments**

First we had grown stoichiometric *a*-SiO₂ layers of thickness 2.0 μm on Si(100) wafers by wet thermal oxidation and then implanted at liquid nitrogen temperature with 2.0

meV $^{74}\text{Ge}^+$ ions to a fluence of $1 \times 10^{17} \text{ cm}^{-2}$. The Ge peak concentration was $\sim 3.0 \text{ at.}\%$ according to a SRIM2008 calculation, and the projected range was $\sim 1.4 \mu\text{m}$ into the *a*-SiO₂ layer, as verified by Rutherford-backscattering (RBS) measurements. Posterior thermal annealing in a conventional furnace under flowing forming gas (5% H₂ in N₂) induced Ge NC precipitation and growth. We obtained four different Ge NC distributions with mean sizes of 4.0, 5.0, 6.0, and 9.0 nm ($\pm 5\%$) by varying the annealing temperature and time [as determined from small-angle x-ray scattering and transmission electron microscopy (TEM) measurements]. Further detail can be found elsewhere.¹¹

After that we irradiated the samples containing Ge NCs of 5.0, 6.0, and 9.0 nm mean diameters at liquid nitrogen temperature with 5.0 meV $^{28}\text{Si}^{+3}$ ions in the fluence range of 1×10^{11} to $2 \times 10^{15} \text{ cm}^{-2}$, to reproduce the conditions previously studied for the 4.0 nm Ge NCs.¹² The projected range for 5.0 meV Si in *a*-SiO₂ is 3.3 μm as given by SRIM2008,¹³ so that no Si ions stay in the NC-containing *a*-SiO₂ layer, consistent with the MD simulations described in Sec. II B. The energy of the Si ions when they reach the depth of $\sim 1.4 \mu\text{m}$ (center of the Ge distribution) is about 2.2 meV. This corresponds to electronic and nuclear energy losses of 173.0 and 4.5 eV/Å in *a*-SiO₂ and 190.0 and 7.0 eV/Å in Ge, respectively, as calculated with SRIM2008 (Ref. 13) (the SRIM electronic stopping power was rescaled to reproduce the experimental range and concentration as measured by RBS).

Prior to XAS measurements we removed the Si substrate by mechanical grinding and wet chemical etching in potassium hydroxide to eliminate reflections from the substrate. In order to improve the signal-to-noise ratio we then stacked several *a*-SiO₂ layers with the Ge NCs together between Kapton tape. We also prepared bulk crystalline and amorphous Ge standards (c-Ge and a-Ge, respectively) appropriate for fluorescence measurements by molecular-beam epitaxy and ion implantation.¹¹ A crystalline GeO₂ (c-GeO₂) standard was prepared by fine grinding bulk c-GeO₂ and mixing with boron nitride to a suitable dilution.

Fluorescence-mode XAS measurements at the Ge *K* edge (11.103 keV) were performed at beamline 20-B of the Photon Factory, Japan. We recorded experimental spectra with a 6×6 pixel array Ge detector and kept the samples at 15 K to minimize the thermal contribution to the disorder in the distribution of interatomic distances. The Si(111) monochromator was detuned by 50% for harmonic rejection. For energy calibration we measured a c-Ge reference foil concomitantly in transmission mode at the back ionization chamber. Under this setup we also performed a series of temperature-dependent extended x-ray absorption fine structure (EXAFS) measurements in the range of 15–300 K for the sample containing 9.0 nm Ge NCs irradiated with Si to a fluence of $2 \times 10^{14} \text{ cm}^{-2}$.

We first averaged and energy calibrated the raw XAS spectra to the reference c-Ge foil signal using the AVERAGE program.¹⁴ Next, we normalized the spectra in ATHENA (Ref. 15) and performed linear combination fits around the x-ray absorption near-edge structure (XANES) region of the Ge NCs samples. The fitting region was selected from 30 eV below to 100 eV above the absorption edge, using the c-Ge,

a-Ge, and c-GeO₂ spectra as standards to fit each Ge NC spectrum. We extracted the EXAFS oscillations from the experimental spectra by background subtraction (removing the raw absorbance) via the AUTOBK algorithm, as implemented in ATHENA. Then we used the EXAFS signal from the bulk c-Ge standard to refine the values of the energy shift parameter ΔE_0 according to the procedure suggested in Ref. 16. This enabled us to perform the alignment of the wave-number *k* scale of the c-Ge theoretical standard generated by the FEFF8 code¹⁷ for all the samples, thus avoiding errors in the structural parameters due to a poor choice of the edge energy position E_0 . We employed ATHENA and ARTEMIS as graphical user interfaces to analyze the data with the IFEFFIT code.¹⁸ We determined structural parameters, in particular, the Debye-Waller factor (variance σ^2 of the interatomic distance distribution) for the first-nearest-neighbor (NN) shell in all the samples. This parameter can be used as a measure of the degree of amorphization for the direct comparison with the simulation. For *k* space we used a Fourier transform window of the Hanning-type with width 0.8 \AA^{-1} and a range from 4.1 to 14.1 \AA^{-1} . The window defining the fitting region in the non-phase-corrected radial distance *R* space was also of the Hanning-type, with width 0.2 \AA and a range from 1.6 to 2.7 \AA . The FEFF8 code¹⁷ was used to calculate *ab initio* effective scattering amplitudes and phase shifts. We fitted each given data set simultaneously with multiple *k* weightings of 13 to reduce correlations between the fitting parameters. We determined the passive electron reduction factor S_0^2 and the energy shift parameter ΔE_0 from the c-Ge data and kept them constant when fitting the Ge NC samples. We obtained the values $S_0^2 = 0.99 \pm 0.07$ and $\Delta E_0 = 0.3 \pm 1.5 \text{ eV}$. We analyzed the temperature-dependent data for the 9.0 nm Ge NCs irradiated with Si to a fluence of $2 \times 10^{14} \text{ cm}^{-2}$ according to the multiple data set fitting procedure described in Ref. 19.

B. Simulations

To understand the nature of amorphization of elemental semiconductor NCs, we prepared several atomistic models of spherical Ge NCs and Si NCs in the range from 2.4 to 9 nm in diameter embedded into an *a*-SiO₂ cell by the combination of the Monte Carlo Wooten-Weaire-Winer method (BOMC) (Ref. 20) to build a coordination-defect-free amorphous structure of silica and subsequently the classical MD method (PARCAS) (Ref. 21) to insert a nanocrystal and optimize the formed interface. The result of the BOMC code, where the bond topology in *a*-SiO₂ was optimized by using a Keating potential, was then additionally relaxed employing the Watanabe-Samela potential.^{22,23} We used the same potential in the rest of our simulations for *a*-SiO₂ as it had been designed to describe Si-O systems; the Si, Ge, and Ge-Si interactions were accounted for using a Stillinger-Weber potential.^{24,25} Specifically, the Ge interactions from Ref. 24 were scaled to give the correct melting point of Ge, which has also been found to give amorphous zone sizes comparable to experiments.²⁵ To obtain Ge-O interactions, we scaled the SiO₂ potential to give GeO₂ a realistic cohesive energy and bond length.²⁶ The Ge-O bond length was ob-

tained from Ref. 27. Detail on the construction of a -SiO₂ and on the formation of a realistic interface between crystalline and amorphous material can be found elsewhere.²⁸

We simulated the irradiation process as follows. The high-energy ions used in experiments for the irradiation of nanocrystal structures are in the meV range when they reach the depth where the nanocrystal concentration is the highest. Hence the ions pierce through the nanocrystal layer, stopping far beyond it.²⁹ The only effect brought in by energetic ions to the NC layer is a considerable number of self-recoils, which initiate the atomic cascades. To focus the study of radiation damage in the NC on the area of interest, we considered only those cascades which were initiated by self-recoils generated inside or in the close vicinity of the NC. In other words, we considered the sphere centered in the NC center with a radius 1.5 times the radius of the spherical NC where we chose the primary recoils at random. We made this choice, on one hand, to include the recoils of NC and a -SiO₂ atoms and, on the other, to avoid cascades spreading over the periodic boundaries. However, the direction of the chosen recoil depended on its radial position: a recoil from the outer part of the sphere (a spherical shell consisting approximately of the interface, thus including both NC and matrix atoms) was directed randomly but only directions toward the NC were accepted; a recoil from the inner part of the sphere (the NC atoms only) was directed randomly with no additional restriction. In this way, we avoided unnecessary computation of the cascades that would not deposit energy within the NC. In principle, secondary and ternary knock-ons from rejected high-energy recoils may hit the NC and cause damage, but the probability of these events is very low (see below). Therefore, the simulation of the contribution of these events to the damage in NC would be rather inefficient.

By simulating a sequence of cascades we computed the dose accumulation in the NCs; every new recoil started from the results of the previous one. We examined three scenarios of dose accumulation: one in which the recoils always started with a rather low energy of 0.1 keV, in the second we included only the recoils starting from 1 keV, and in the last the cascades were initiated by recoils of the whole range of energies between 5 eV and 5 keV chosen at random from a realistic recoil spectrum obtained by the MDRANGE code.^{30,31} The latter is the closest to the experimental condition as it includes the whole range of primary recoils knocked out by a passing ion. This case was applied only for 4 nm Ge NCs as a model to assess the contribution of low-energy cascades (about the threshold of atom displacement), which constitute the strong maximum in the primary recoil spectrum (Fig. 1). Unfortunately computer capacity limitations prevented us from simulating irradiation of also the larger nanocrystals with the recoil spectra.

We obtained the recoil spectrum with the MDRANGE code³⁰ as follows. In order to take into account the presence of a Ge NC layer, we modeled the matrix as comprised of three layers: two thick layers of silica with a thin layer of germanium between them. The germanium layer in the simulation was placed at the same depth as the experimental maximum of the Ge NC distribution. We simulated 10,000 trajectories of the Si⁺ ion with the energy $E_0=5$ MeV, corresponding to the experimental value inside of the model

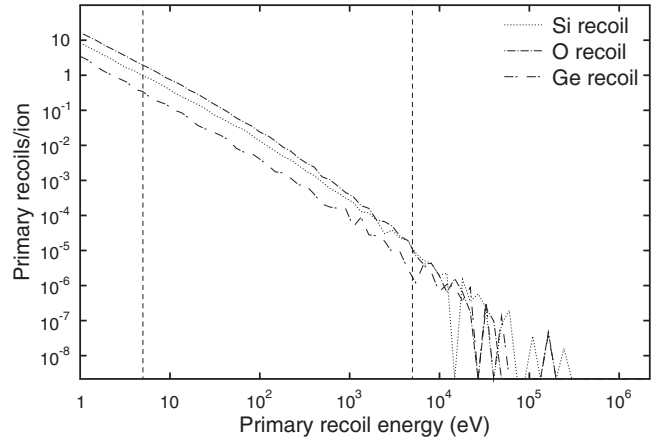


FIG. 1. Full primary recoil spectrum of Si, O, and Ge atoms present in silica with a thin Ge layer in between after Si⁺ irradiation with $E_0=5$ MeV. The dashed lines select the range of recoils used in the simulation.

matrix. In this way, we produced the spectrum of primary recoil energies present in the displacement cascade emerging from the incoming ion (Fig. 1). The probabilities were then modified according to the ratio between the MDRANGE one-dimensional calculation and the volumes from which the recoils were chosen in the present simulations to relate the number of primary recoils to the experimental fluence. We chose the recoil spectrum to include energies between 5 eV and 5 keV, since recoils with energies lower than 5 eV will not displace any other atoms while recoils with more than 5 keV are negligible in number (<0.4%) compared to the rest of the spectrum. Moreover, cascades of energies higher than 5 keV tend to split into subcascades.²⁵ Thus, the damage produced by such recoils is self-similar to the damage from the recoils included in our simulations.

In the monoenergetic recoil cases we included 1 keV cascades, as according to our previous estimations these cascades are mostly developed within the NC even if it has a small size.³² By using also 0.1 keV recoils we aimed to estimate the significance of low-energy cascades, which produce a very localized defect volume resulting in the least atom mixing, since only a few atoms can be displaced in these cascades.

We chose the fluxes such that every cascade had enough time to cool to the equilibrium temperature of the surrounding lattice. Since we used a widely varying range of recoil energies, each event was simulated assuming the quenching time as a linear function of primary recoil energy with the lower limit at 1 ps and the upper limit at 10 ps (Fig. 2). We applied this approach to avoid unnecessarily long MD calculations for the low-energy cascades, verifying the choice of the quenching time by the remaining kinetic energy in the system. In this way, we monitored the temperature in the cell after each cascade, which had been held within 400–600 K, a value much below the melting point of Ge.

The calculations needed to compare simulated and experimental energy deposition scales are presented in Appendix. As discussed there, a quantitative comparison of fluence and dose between simulation and experiments can only be carried out for the recoil spectrum cases.

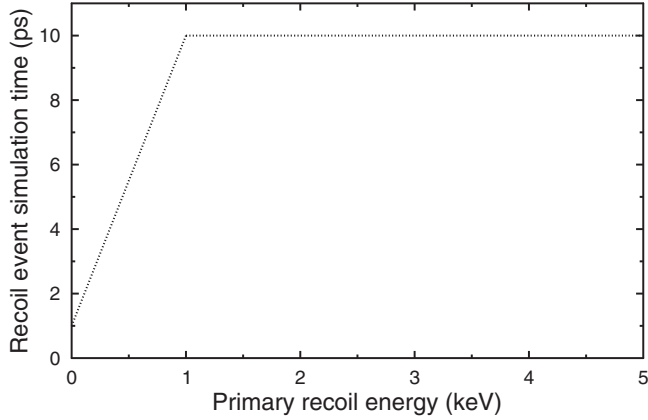


FIG. 2. Simulation time for every cascade as a function of primary recoil energy.

In the simulations we obtain the deposited dose in units of average energy added to the system per atom. In other words, we sum up the velocities of the NC atoms after the cascade and subtract thermal fluctuations to calculate the dose deposited in the NC as follows:

$$E_{tot}^{NC} = E_1^{NC} - E_0^{NC}, \quad (1)$$

where,

$$E_1^{NC} = \frac{1}{2} \sum mv_i^2(\text{at } t=0.2 \text{ ps of each cascade}), \quad (2)$$

$$E_0^{NC} = \frac{1}{2} \sum mv_{i0}^2 - E_{rec}^{NC}(\text{at } 0 \text{ ps of each cascade}). \quad (3)$$

Since the dose of deposited energy is measured only within the NC, we subtracted the energy of the primary recoil from E_0^{NC} if it had been chosen among the NC atoms.

We followed the evolution of the amorphization process by applying the angular structure factor analysis method, as in Ref. 33, reparametrized to include also second-nearest neighbors to be more sensitive. In the present work, comparing the average structure factor of the NC atoms after irradiation to the structure factor of bulk crystalline and bulk amorphous Ge and Si, respectively, we obtain the fraction of NC atoms, which have amorphous environments, or how much each NC has currently been amorphized.

To ensure that the faster amorphization of embedded NCs is not a question of analysis method, we simulated the amorphization of bulk Ge as well. We proceeded the amorphization of initially crystal bulk Ge by ion irradiation by simulating successive 100 eV primary self-recoils at 300 K temperature. We chose the cell size of cubic crystalline Ge sufficiently large (4.5 nm, 4096 atoms with periodic boundary conditions) to contain the cascade initiated by a recoil inside the cell boundaries.

We simulated amorphization by successive self-recoils exploiting the following repetitive pattern. At first, the cell was shifted randomly to initiate the recoil in a random position relative to the crystal, but always at the center of the simulation volume. Then, we selected the Ge atom closest to

the center of the simulation cell to be a recoil with 100 eV energy in a random direction. The duration of the cascade development of each recoil was fixed to 10 ps. In this case, we also monitored the temperature by cooling the 5 Å next to the borders to 300 K during the first 9 ps, and in the final 1 ps the whole cell was cooled to ensure that the start of the next recoil was always at the same temperature. After the recoil, we enabled pressure relaxation in the simulation cell for 3 ps at 300 K.

The pattern was repeated 1,000 and 800 times for the first and second series, respectively. Analysis of the degree of amorphization as a function of irradiation dose showed that in both simulation series the Ge cell was fully amorphized after about 700 recoils, i.e., after a dose of about 17 eV/atom.

Interestingly, test runs with no pressure control showed that—at least in the currently used potential—when the cell size was kept constant at the equilibrium value for the perfect crystal, the system never amorphized but obtained a steady-state defect concentration fluctuating around roughly 10%. The system was then at high pressures around 50 kbar, indicating that a high-pressure state can enhance defect recombination.

III. RESULTS AND DISCUSSION

A. Experiments

Since the XANES and EXAFS regions of a XAS spectrum contain different information, we use them both in a complementary manner to probe the amorphization of Ge NCs. XANES provided information from linear combination fits using measured bulk standards (no theoretical input involved), where we probed the amorphization by the gradual disappearance of multiple-scattering effects stemming from the ordered atomic arrangement in the crystalline phase. EXAFS, on its turn, provided detailed structural information through comparison of the isolated single-scattering signal from the first NN shell to the theoretical standard generated by the FEFF8 code.

In this case, we probed the amorphization by the evolution of the fitted EXAFS Debye-Waller factor σ^2 , which we employ here as an indication of the total disorder in the atomic arrangement.

1. XANES results

In Figs. 3(a)–3(d) we present the normalized XANES spectra obtained for the bulk standards as well as the unirradiated and irradiated Ge NCs samples. While the c-Ge and c-GeO₂ spectra in Fig. 3(a) show several features arising from multiple scattering of the photoelectrons in the ordered arrangement of neighboring atoms, the a-Ge spectrum is rather flat reflecting the higher disorder in atomic positions. We use the solid dark gray arrows in Fig. 3(a) to indicate characteristic features of the electronic structure of a Ge-O environment: an increase in the height of the white line (peak in the spectrum just after the absorption edge) and a wide depression at ~ 11145 eV. The same arrows in Figs. 3(b)–3(d) indicate some Ge-O bonds formed at higher irradiation fluences as a result of intermixing at the NC/matrix

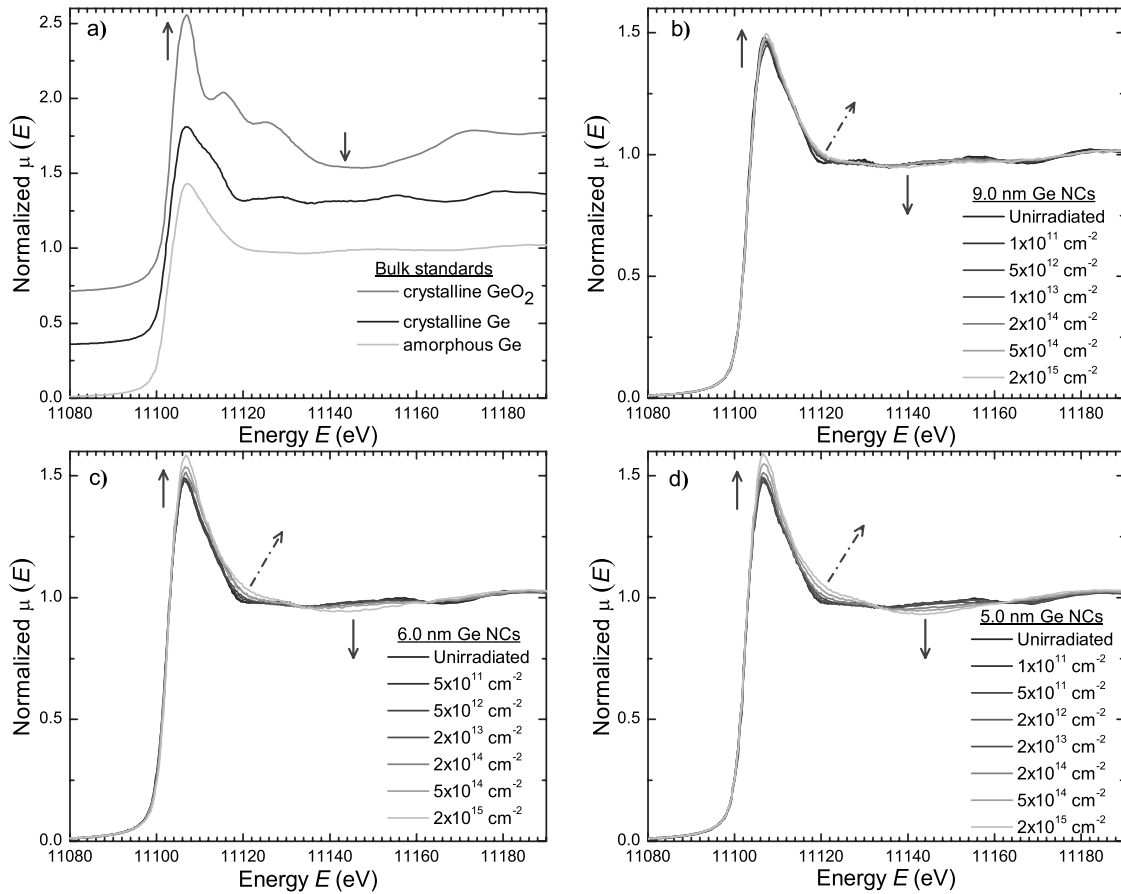


FIG. 3. XANES region of the XAS spectra for (a) bulk standards, (b) 9.0 nm Ge NCs, (c) 6.0 nm Ge NCs, and (d) 5.0 nm NCs. The arrows indicate regions of the spectra, where a progressive change with irradiation fluence is evident due to the reasons commented on the text. Not all irradiation fluences are shown and the bulk spectra have been offset for clarity.

interface and/or displacement of Ge atoms from the interior of the NCs causing their dissolution. This effect is more pronounced for 5.0 nm [Fig. 3(d)] than for 9.0 nm [Fig. 3(b)] Ge NCs and is only appreciable at fluences higher than those needed to amorphize the NCs. This observation is in a good agreement with the simulations presented herein, as will be discussed below, and with the transmission electron microscopy results for smaller (4.0 nm) Ge NCs presented in Ref. 12. The dash-dotted dark gray arrows in Figs. 3(b)–3(d) indicate a progressive change from a c-Ge to an a-Ge configuration at lower fluences and then to a Ge-O configuration at higher fluences.

The fractions of crystalline, amorphous, and Ge-O environments for unirradiated and irradiated Ge NCs as determined from linear combination fits to the XANES data are presented in Fig. 4. Triangles, squares, and circles correspond to 9.0, 6.0, and 5.0 nm Ge NCs, respectively. Full lines and open symbols correspond to the c-Ge fraction, dashed lines and filled symbols correspond to the a-Ge fraction, while dotted lines and half-filled symbols correspond to the Ge-O fraction. The unirradiated Ge NCs already present an initial a-Ge fraction, which is higher for smaller sizes, due to the disorder at the NC surface/interface with the matrix as previously discussed in Ref. 11 and neatly illustrated here in the MD simulation shown in Fig. 8.

From Fig. 4 the complete amorphization of all NCs in the ensembles (i.e., where c-Ge fraction reaches 0 and a-Ge frac-

tion peaks) happens at 2×10^{13} , 5×10^{13} , and 2×10^{14} cm^{-2} for the 5.0, 6.0, and 9.0 nm Ge NCs, respectively. TEM results and MD simulations reinforce that at such fluences the NCs are still spherical and no size change or dissolution takes place. This is important since it has been shown that for very small (< 2.0 nm diameter) NCs a linear combination fit using bulk standards might be inappropriate.³⁴

As the irradiation fluences become higher than the values listed above, a Ge-O fraction becomes apparent and reaches 25, 20, and 12% for 5.0, 6.0, and 9.0 nm Ge NCs, respectively, at 2×10^{15} cm^{-2} . It should be pointed out that the Ge-O bonds formed after irradiation most likely correspond to amorphous or molecularlike GeO_2 rather than crystalline GeO_2 . Thus, having an amorphous rather than a crystalline GeO_2 bulk standard for the linear combination fits will be, in principle, preferable. However, due to the fact that the monitored XANES features depend on the characteristic electronic configuration of a Ge-O bond (unlike the features used to monitor the c-Ge to a-Ge transformation, which depend on multiple-scattering effects from ordered atomic positions), we can consider using c- GeO_2 here as a reasonable approximation.

We will further discuss the results obtained from the XANES analysis in Sec. III A, where we compare them to the outcome of the EXAFS data analysis.

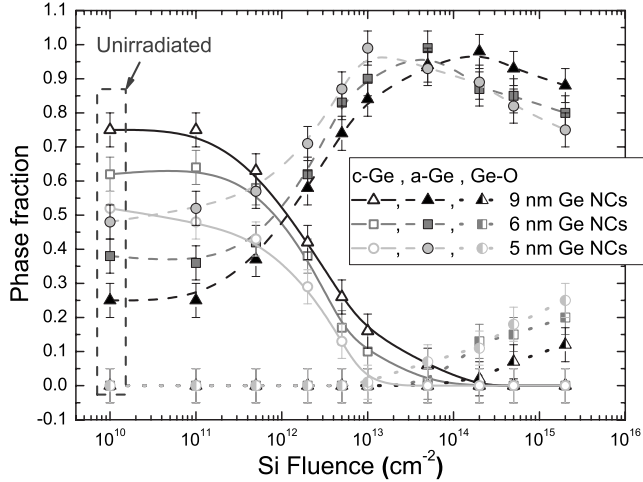


FIG. 4. Fractions of c-Ge, a-Ge, and Ge-O environments for unirradiated and irradiated Ge NC distributions plotted as a function of Si irradiation fluence. Triangles, squares, and circles correspond to 9.0, 6.0, and 5.0 nm mean diameter Ge NCs, respectively. Full lines and open symbols correspond to the c-Ge fraction, dashed lines and filled symbols correspond to the a-Ge fraction, while dotted lines and half-filled symbols correspond to the Ge-O fraction.

2. EXAFS results

We present the k^2 -weighted EXAFS oscillations for bulk standards and Ge NC samples in Figs. 5(a)–5(d). We also plot the corresponding non-phase-corrected Fourier transforms in Figs. 5(e)–5(h). While the c-Ge and c-GeO₂ oscillations in Fig. 5(a) show a complex pattern resulting from the interference of signals from the various NN shells (plus multiple-scattering contributions), visible as peaks in Fig. 5(e), the a-Ge oscillations appear comprised of a single frequency, corresponding to the single first NN peak in the Fourier transform. The absence of higher NN shells in the EXAFS signal due to structural disorder is a characteristic feature of amorphous materials.^{9,35}

The right arrow in Fig. 5(e) indicates this absence of higher shells for bulk a-Ge while the left arrow indicates the decrease in amplitude of the first NN signal relative to bulk c-Ge mainly due to the higher structural disorder (the EXAFS Debye-Waller factor σ^2 is twice as big as for c-Ge) and to a lesser extent due to the small decrease in mean coordination number from 4.0 to 3.9 atoms.¹²

Figures 5(b)–5(d) show a progressive washing out of the complex interference pattern in the EXAFS of the Ge NCs as the Si irradiation dose increases. The smaller the NCs [going from Figs. 5(b)–5(d)], the lower the irradiation fluence where the spectra become very similar to the single-frequency EXAFS spectrum of bulk a-Ge shown in Fig. 5(a). This can be further inferred from the Fourier transforms in Figs. 5(f)–5(h), taken over the window delimited by the vertical dashed lines plotted in Fig. 5(d). Three peaks are clearly visible in the spectra of the unirradiated Ge NCs, corresponding to the first NN shell (~ 2.1 Å) as well as to the second (~ 3.6 Å), and the third (~ 4.3 Å) NN shells superimposed on the signal of multiple-scattering paths.³⁶ We use the same scale in Figs. 5(f)–5(h) to illustrate the decrease in peak am-

plitudes for the unirradiated samples with decreasing mean NC size, as a result of the finite-size effects verified in the MD section and in Ref. 11, i.e., the decrease in coordination number and the increase in structural disorder at the NC/matrix interface as the NCs become smaller [from Figs. 5(f)–5(h)].

The right arrows in Figs. 5(f)–5(h) highlight the strong decrease in amplitude of the second NN shell upon irradiation: for the 9.0 nm Ge NCs the signal is almost gone after 1×10^{13} cm⁻², while for the 6.0 and 5.0 nm NCs the same happens at the lower fluences of 5×10^{12} and 2×10^{12} cm⁻², respectively. Irradiation at higher fluences completely washes out the signals from higher NN shells, but it should be pointed out that not all NCs in the ensembles are actually amorphized at the fluences where the second NN signal starts to disappear, as it is shown below. The left arrows in Figs. 5(f)–5(h) point out the decrease in amplitude of the first NN shell peak with increasing Si irradiation fluence, thanks initially to the amorphization of the NCs (increase in Debye-Waller factor due to higher structural disorder) and then to the intermixing of NC and matrix atoms (reduction in coordination number/NC dissolution) as revealed by the fitting procedure. We summarize our results on the obtained Debye-Waller factors and coordination numbers as a function of irradiation fluence in Figs. 6(a) and 6(b), respectively. We obtained such values by isolating and fitting the signal of the first NN shell as described in Sec. II.

In Fig. 6(a) one can see that the initial value of the Debye-Waller factor is different for the Ge NCs and is highest for the smallest NCs, which happens due to finite-size effects, as mentioned above and discussed in detail in Ref. 11. As the Si irradiation fluence increases, the Debye-Waller factor approaches the value for bulk a-Ge and complete amorphization is achieved between 2 and 5×10^{13} cm⁻² for the 5.0 nm Ge NCs, between 5×10^{13} and 1×10^{14} cm⁻² for the 6.0 nm NCs, and between 1×10^{14} and 2×10^{14} cm⁻² for the 9.0 nm NCs. This observation is in excellent agreement with the XANES results. Irradiation with higher fluences up to 2×10^{15} cm⁻² does not change significantly the Debye-Waller factors of the Ge-Ge first NN shell. Nevertheless, the peak amplitudes in the Fourier transforms in Figs. 5(f)–5(h) continue to decrease, due now to a decrease in coordination number, as verified from Fig. 6(b). Irradiation at fluences below those needed for complete amorphization of all NCs in the ensembles does not affect the coordination number for all samples, indicating no size changes at this regime. At the amorphization fluences determined from XANES and EXAFS for the 5.0, 6.0, and 9.0 nm Ge NCs, we observed a very small decrease in coordination number, which corroborates the complete amorphization of all NCs in the ensembles, since a-Ge presents slightly smaller coordination than c-Ge. At fluences higher than those needed for amorphization we found a significant drop in coordination number, which is more pronounced for the ensemble with the smaller Ge NCs (5.0 nm). Such a drop in coordination number evidences a decrease in number of Ge-Ge bonds due to intermixing of NC and matrix atoms and the consequent reduction in NC size followed by their dissolution.

Interestingly enough, EXAFS spectra of the irradiated Ge NCs do not indicate any significant presence of Ge-O bonds,

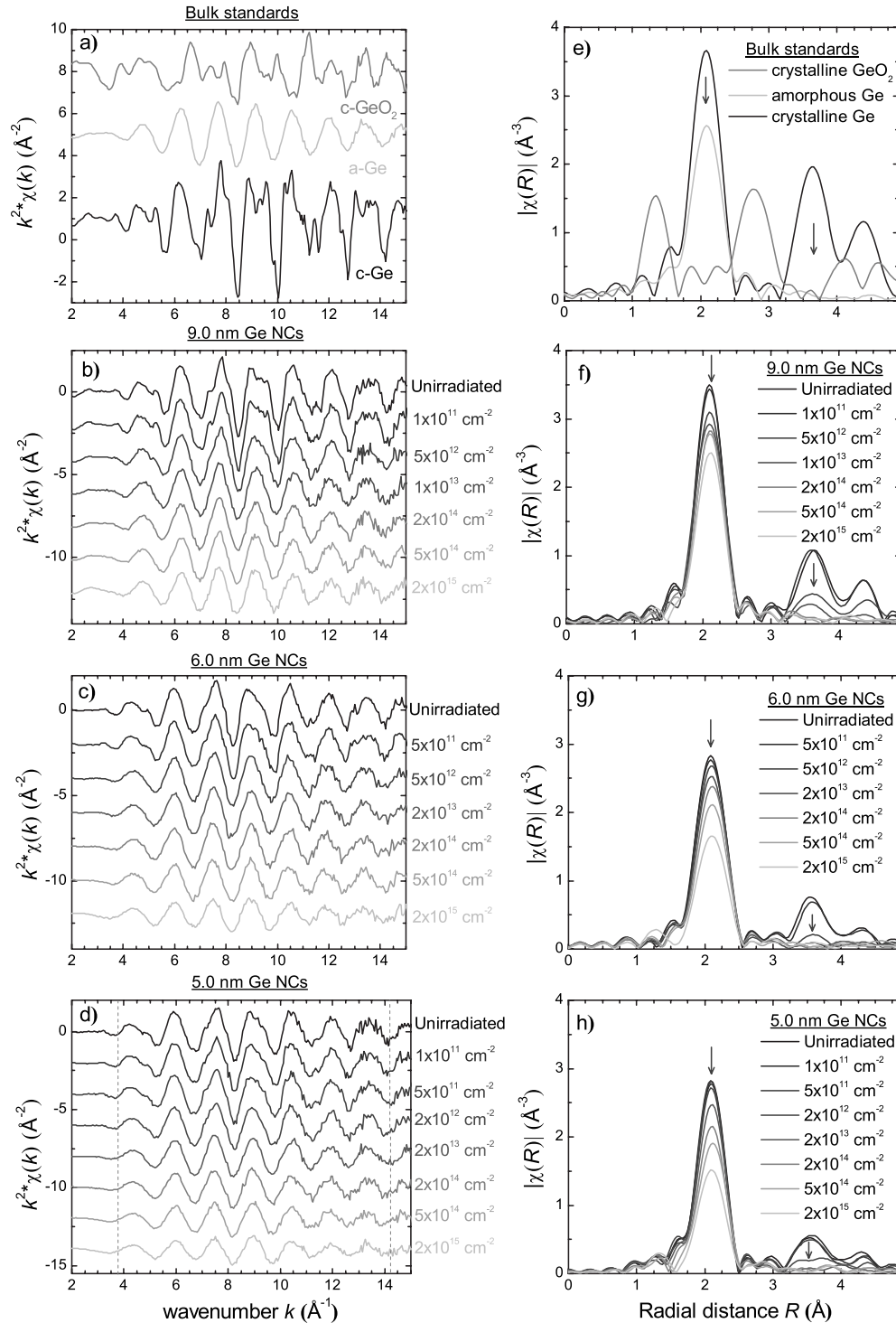


FIG. 5. (a)–(d) k^2 -weighted EXAFS oscillations (left column) and (e)–(h) corresponding Fourier transforms (right column) obtained from the range delimited by the dashed vertical lines in (d). Spectra on the left column were shifted for clarity. Panels (e) to (h) were plotted in the same scale to enable comparison between the amplitudes of the peaks for all samples.

unlike the XANES data. We see no clear peaks (apart from a very small hump in the spectra for the smaller Ge NCs irradiated with $2 \times 10^{15} \text{ cm}^{-2}$) in the Fourier transforms of Figs. 5(f)–5(h) at the position of $R \sim 1.3 \text{ \AA}$, where the first Ge-O NN shell appears for the bulk c-GeO₂ standard in Fig. 5(e). We explain this as a result of two main factors: O atoms have weaker effective scattering amplitude than Ge, especially at

higher k values, and the Ge-O bonds in our samples are formed by the intermixing of NC and matrix atoms, resulting in a highly disordered phase with much lower coordination number and higher Debye-Waller factor relative to c-GeO₂. Such combination flattens out the Ge-O peaks to an extent that they are not observable in the Fourier transforms. Nevertheless, the presence of Ge-O bonds is indirectly confirmed

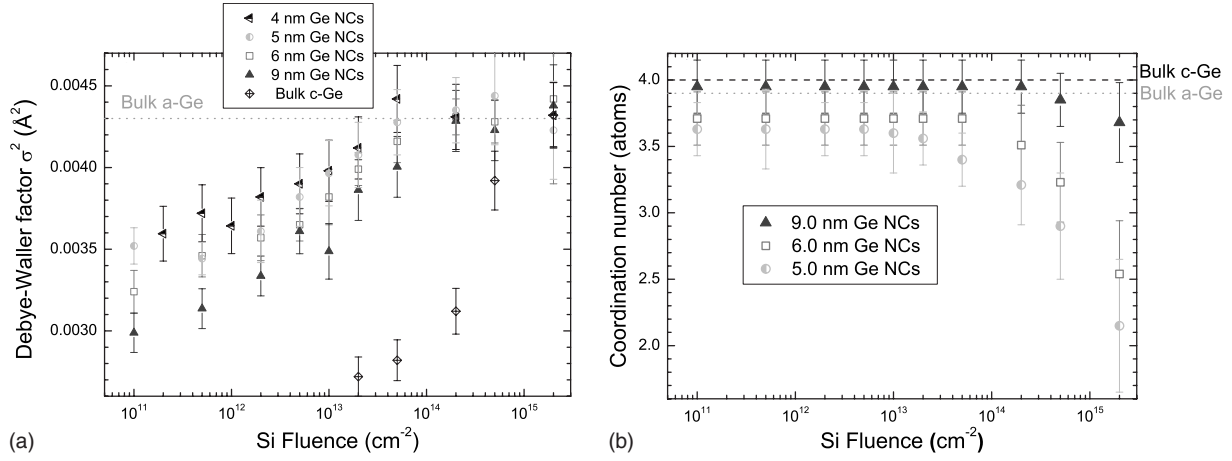


FIG. 6. (a) Variation in the Debye-Waller factors and (b) the mean coordination number of the Ge NC ensembles as a function of Si irradiation fluence. The dashed and dash-dotted lines indicate the values for bulk c-Ge and a-Ge, respectively. Symbols correspond to values measured from experimental data and solid lines are just guides to the eyes.

from EXAFS data by the decrease in number of Ge-Ge bonds upon irradiation [Fig. 6(b)], which is too steep to be the result of only a decrease in mean NC sizes without NC dissolution/intermixing with the α -SiO₂ matrix.

Further evidence that amorphization of the Ge NCs was achieved at the fluences mentioned herein is provided by temperature-dependent EXAFS measurements performed for the sample containing 9.0 nm Ge NCs irradiated with Si to a fluence of $2 \times 10^{14} \text{ cm}^{-2}$. From such measurements we separated the structural and thermal contributions to the total disorder in the interatomic distance distribution and extracted the mean vibrational frequency of the Ge-Ge bonds as given in terms of an Einstein frequency ω_E or Einstein temperature Θ_E .^{11,37} In Fig. 7 we show the evolution of the Debye-Waller factor with the measurement temperature (symbols) and the fit to the data with the Einstein model (line). Detail on the analysis procedure and the Einstein model can be found elsewhere.^{11,37} The obtained structural contribution to the to-

tal disorder σ_{static}^2 was $(2.3 \pm 0.1) \times 10^{-3} \text{ \AA}^2$, amounting to about twice that observed for unirradiated 9.0 nm Ge NCs in Ref. 11. The thermal contribution to the total disorder, given in terms of the Einstein temperature Θ_E , increased with temperature at a faster rate than that observed for the unirradiated 9.0 nm Ge NCs in Ref. 11, yielding $\Theta_E = 347 \pm 7$ as opposed to $\Theta_E = 352 \pm 4$ for the unirradiated NCs.¹¹ A similar decrease in Einstein temperature is evident when we compare results for bulk c-Ge ($\Theta_E = 351 \pm 7$) and bulk a-Ge ($\Theta_E = 343 \pm 4$).¹¹ Thus, both the static and thermal contributions to the total disorder obtained for the irradiated 9.0 nm Ge NCs indicate that complete amorphization is achieved. It is interesting to point out that both unirradiated and irradiated Ge NCs present slightly higher Θ_E values when compared to the respective bulk phases. This is probably an indication that finite-size effects and/or the presence of the α -SiO₂ matrix further influence the mean vibrational frequency of the Ge-Ge bonds in the NCs.

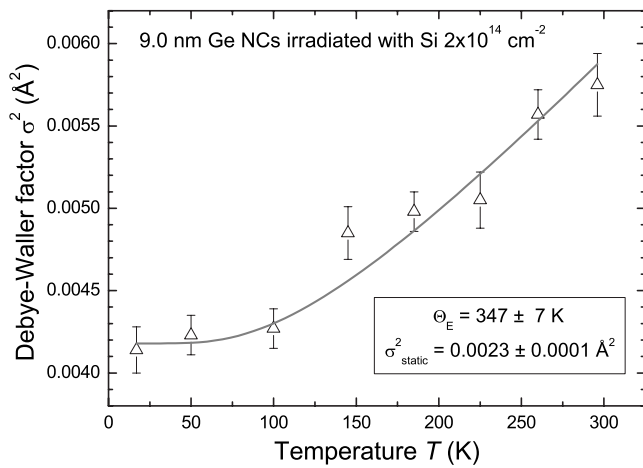


FIG. 7. Evolution of the EXAFS Debye-Waller factor with measurement temperature for the sample containing 9.0 nm Ge NCs irradiated with Si to a fluence of $2 \times 10^{14} \text{ cm}^{-2}$. Symbols are experimental data and the line is the fit with the Einstein model described in Refs. 11 and 37.

B. Comparison of experiment and simulation

To demonstrate the difference in NC structure before and after ion irradiation, we compare the unirradiated and amorphized atomistic models of the same 4 nm Ge NCs in Fig. 8. We observed similar structural changes for the other NCs

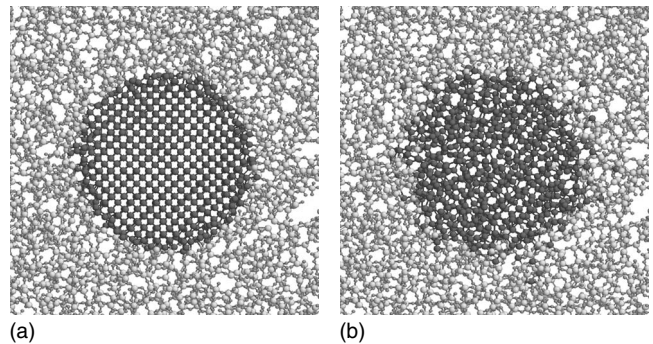


FIG. 8. Cross section of a 4 nm NC before and after irradiation

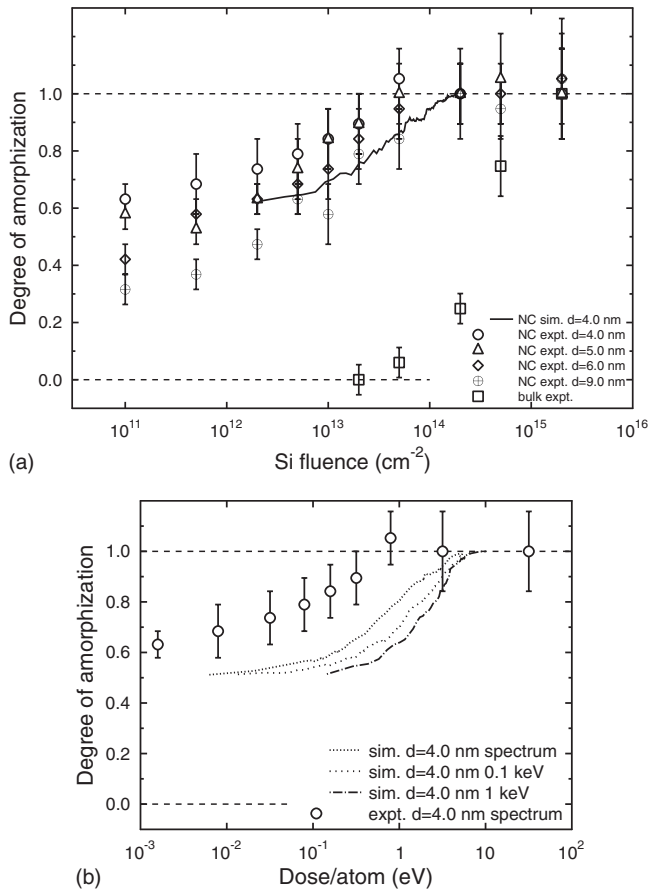


FIG. 9. Comparison of simulated and experimental amorphization rates for Ge NCs and bulk Ge. (a) Comparison as a function of fluence and (b) comparison as a function of dose for the recoil spectrum case. Also shown in plot (b) is the amorphization rate for 0.1 and 1 keV recoils.

studied in the present work. The interface of the initially crystalline NC is a narrow well-defined border separating it from the amorphous silica matrix. The atom mixing during the irradiation brings in some matrix atoms, but only very small nanocrystals tend to dissolve almost completely, while the big nanocrystals remain separated from the matrix even after the structure is rendered fully amorphous.

Since the Debye-Waller and structural factors have a similar concept of a measure of averaged disorder around every single atom within a NC, we introduce the unitless parameter, called “degree of amorphization” in order to make experimental and simulation results comparable. Thus, we can compare the unitless structural factors to the relative Debye-Waller factors, for which the values of 0 and 1 correspond to the Debye-Waller factors of bulk c-Ge and bulk a-Ge [Fig. 6(a)], respectively. However, as described in detail in Appendix, a direct comparison with experimental fluences can be made only for the recoil spectrum case. This comparison is shown in Fig. 9(a) for the fluences, and Fig. 9(b) for the doses. Figure 9(b) also shows, for comparison, the 100 eV and 1 keV monoenergetic cases, which clearly differ from the recoil spectrum case because most low-energy recoils in the spectrum case do not deposit any energy to the nanocrystal, as discussed in Appendix. The recoil spectrum cases are,

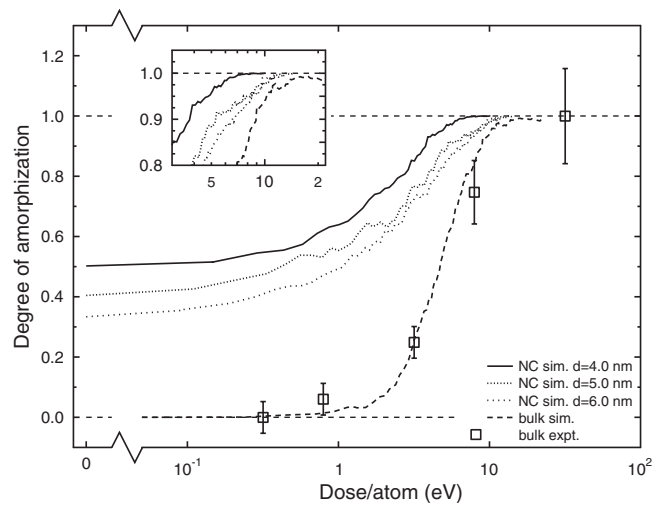


FIG. 10. Comparison of degree of amorphization of the Ge NCs of different sizes obtained by simulation of ion irradiation (1 keV monoenergetic recoil case) as a function of the absorbed irradiation dose per atom. Also shown are the simulated and experimental bulk results.

on the other hand, in good agreement with experiments, both in units of fluence and dose.

In Fig. 10 we summarize the simulated Ge results obtained for the NCs in the size range from 4 to 6 nm. We also added the curve of amorphization for bulk Ge crystal. Comparison with Fig. 8(a) shows that both in the case of experiments and simulations, the smallest nanoclusters amorphize the easiest, and in both cases there is a dramatic (roughly one order of magnitude) difference between the dose needed to amorphize the nanoclusters and bulk Ge. Surprisingly, also the 9 nm NCs, which could be considered as quite large nanocrystals, still show clear finite-size properties (Fig. 6), although the amorphization dose in this case is slightly closer to that for bulk Ge.

The size of the NC is clearly an important factor, as it can be seen from both the experimental and simulated results that the smaller NCs are already initially in a disordered state. Due to their partly amorphous structures, there are plenty of seeds of crystal disorder, and the amorphization dose is significantly lower than that for bulk Ge. The difference between the two methods seems to be the initial state of the NCs. The atomistic model predicts the NCs to be initially slightly more crystalline than the EXAFS measurements do, which explains the somewhat higher irradiation dose needed to amorphize the NCs in the simulations. We assign this small discrepancy to the greater number of inherent defects at the interface probably present in the experimental case. Since in the simulations we insert a nanocrystal cut out from a perfect bulk crystal, all the defects at the interface appear during the optimization process. In the experiments, the formation of NCs is known to involve a molten stage and posterior crystallization, during which additional stresses might be induced, thus increasing the number of interface defects.

Another interesting conclusion can be derived from Fig. 11, where we plot both Si and Ge NCs of the same sizes versus irradiation dose. Here we compare only simulation results since EXAFS analysis of amorphized Si NCs is not

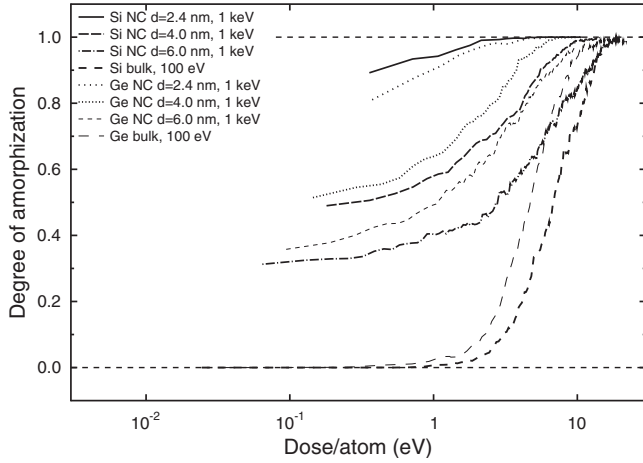


FIG. 11. Amorphization of Si and Ge NCs and bulk of different sizes as a function of absorbed irradiation dose per atom. The Ge curves are thinner than the Si ones.

available. Nevertheless, we can clearly see the difference in the amorphization process, which can be explained by the difference in the interface structures of Si and Ge NCs. A striking feature of this analysis is that while for the smallest diameter (2.4 nm) the Si NCs are rendered amorphous faster than the Ge NCs, for bigger sizes this ratio reverses and the Ge NCs become easier to amorphize compared to Si NCs of the same size. We explain this by the effect of the interface, which extends deeper inside of the Ge NCs, as it can be seen in Fig. 12, where we plot the radial distribution of potential energy per atom in unirradiated Si and Ge NCs. The results have been statistically averaged over 10 structures for each size. The interface of the small Si NCs (2.4 nm) contains the largest amount of ill-coordinated atoms, but the size of the NC does not allow for full compensation of this disturbance by torsion of the crystal structure. For the other NCs (including 2.4 nm Ge NCs) this process seems to be fulfilled as the maximum of all the curves remains the same, while the area under the curves is visibly reducing. We also observe another peculiarity of this analysis, namely, that the Si NCs form

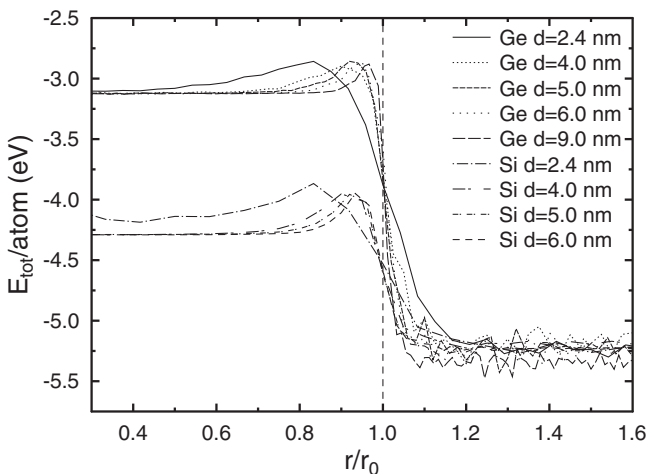


FIG. 12. Potential energy of atoms as a function of distance to the center in arbitrary units.

better localized interfaces with *a*-SiO₂ compared to Ge NCs, which makes the amorphization process slightly delayed. In Fig. 11 we also plotted the amorphization curve for bulk Si and Ge. For both Si and Ge, nanocrystals amorphize easier than the bulk for all studied sizes. The easier amorphization of bulk Ge compared to bulk Si, especially in the lower-dose parts of the curve, can be understood in terms of the well-established observation that amorphous clusters produced under similar irradiation conditions in Ge are larger than those in Si,^{25,38} thus causing higher damage levels at least when damage overlap is not complete.

In general, the fact that our classical simulations (electronic effects are not included explicitly) reproduce the experiments fairly well provides strong evidence that the easier amorphization of NCs is not related to the change in their electronic properties. Thus, the results show that the experimental observations can be well explained by the interface (and defects in it) weakening the mechanical stability of the embedded particles.

IV. CONCLUSIONS

Using a combination of molecular dynamics (MD) simulations and XAS measurements, we have shown that the amorphization of Si and Ge nanocrystals is reached at doses roughly one order of magnitude lower than those for the bulk crystals. Examining nanocrystals in the size range from 2.4 to 9 nm, we have also shown that the susceptibility to amorphization decreases with increasing nanocrystal size. Our analysis has shown that the easier amorphization is due to the interface and defects in it weakening the nanocrystal mechanically. Potential-energy analysis showed that the weakening extends quite deep inside the nanocrystals. Surprisingly, the finite-size effect remains significant also for the largest nanocrystals of 9 nm.

APPENDIX: CORRESPONDENCE OF FLUENCE AND DOSE SCALES

The calculations of simulated and experimental fluence and dose scales are complicated by the fact that the nanoclusters do not form a continuous layer. For a given depth, many ions will not hit a single nanocrystal at that depth. Note that the peak Ge concentration was only $c_{Ge}=0.03$, see Sec. II A.

1. Area covered by nanoclusters at given depth

We calculate the area fraction f_A (out of the total irradiated area) occupied by nanoclusters of radius r at a given depth region as follows. Consider a slab of thickness $2r$ centered on the nanocluster. A single nanocluster with radius r has a volume $V_{nc}=4\pi r^3/3$. The volume of a cube surrounding this sphere is $V_{cube}=(2r)^3$. This cube is surrounded by a silica area of arbitrary shape with no nanoclusters A , which has the volume $V_A=2rA$. To get the desired Ge concentration, we need to have

$$\begin{aligned}
c_{\text{Ge}} &= \frac{V_{nc}\rho_{\text{Ge}}}{V_{\text{silica}}\rho_{\text{SiO}_2}} \\
&= \frac{V_{nc}\rho_{\text{Ge}}}{(V_{\text{cube}} - V_{nc} + V_A)\rho_{\text{SiO}_2}} \\
&= \frac{4\pi r^3/3}{[(2r)^3 - 4\pi r^3/3 + 2rA]}\frac{\rho_{\text{Ge}}}{\rho_{\text{SiO}_2}}, \quad (\text{A1})
\end{aligned}$$

where ρ_{Ge} and ρ_{SiO_2} are the atomic densities of bulk Ge and amorphous SiO₂, respectively. Solving for A gives

$$\begin{aligned}
A &= \frac{\frac{\rho_{\text{Ge}}}{\rho_{\text{SiO}_2}} \frac{4\pi r^3/3}{c_{\text{Ge}}} - (2r)^3 + 4\pi r^3/3}{2r} \\
&= \frac{\frac{\rho_{\text{Ge}}}{\rho_{\text{SiO}_2}} \frac{2\pi r^2/3}{c_{\text{Ge}}} - (2r)^2 + 2\pi r^2/3, \quad (\text{A2})
\end{aligned}$$

and thus the fraction of area where the ion hits a nanocluster becomes

$$\begin{aligned}
f_A &= \frac{A_{nc}}{A_{\text{cube}} + A} = \frac{\pi r^2}{(2r)^2 + \frac{\rho_{\text{Ge}}}{\rho_{\text{SiO}_2}} \frac{2\pi r^2/3}{c_{\text{Ge}}} - (2r)^2 + 2\pi r^2/3} \\
&= \frac{\pi}{\frac{\rho_{\text{Ge}}}{\rho_{\text{SiO}_2}} \frac{2\pi/3}{c_{\text{Ge}}} + 2\pi/3} = \frac{1}{\frac{\rho_{\text{Ge}}}{\rho_{\text{SiO}_2}} \frac{2/3}{c_{\text{Ge}}} + 2/3}, \quad (\text{A3})
\end{aligned}$$

which inserting $\rho_{\text{Ge}}=44 \text{ at/nm}^3$ and $\rho_{\text{SiO}_2}=66 \text{ at/nm}^3$ gives $f_A=0.0645$.

2. Conversion of number of recoils to fluence

For the recoil spectrum cases, the simulated number of recoils was recalculated into an experimental fluence by taking this relative area into account as follows. We first used MDRANGE simulations to deduce the number of recoils in the energy interval of 5 eV–5 keV (c.f. Sec. II B) per length $N_{\text{rec},l}$. We simulated the passage of 5 meV Si ions through silica, placing a 5 nm Ge layer between the silica at a depth of 1.4 μm as in the experiments. We then calculated the average length that an ion hitting a random position in a spherical cluster will pass through in it l .

Thus N_{rec} recoils simulated with MD in the Ge cluster corresponds to

$$N_{\text{ion}} = \frac{N_{\text{rec}}}{N_{\text{rec},l}} \quad (\text{A4})$$

ions that hit the cluster. However, not all ions hit a cluster at a particular depth, but we must consider that a fraction of f_A of the ions miss it. Thus the effective area ions passing through per single cluster is $A^* = \pi r^2/f_A$ and we obtain for the correspondence between the number of recoils in the MD cascade simulation and the fluence

$$\Phi = \frac{N_{\text{ion}}}{A^*} = \frac{N_{\text{rec},l}}{\pi r^2/f_A} = \frac{N_{\text{rec},l}}{\frac{\rho_{\text{Ge}}}{\rho_{\text{SiO}_2}} \frac{2/3 \pi r^2}{c_{\text{Ge}}} + 2/3 \pi r^2}. \quad (\text{A5})$$

The MDRANGE calculations gave $N_{\text{rec},l}=0.1029$ recoils/nm and using $l=2.67 \text{ nm}$ for $r=2 \text{ nm}$ and $f_A=0.0645$ gives that one MD recoil $N_{\text{rec}}=1$ corresponds to 1.87×10^{12} ions/cm². Naturally this conversion can only be carried out for the recoil spectrum case, since for the monoenergetic recoils one cannot obtain $N_{\text{rec},l}$.

3. Conversion of fluence to dose

As an independent calculation of the correspondence between experiment and simulations, we also estimated how the experimental fluence translates to dose.

To convert the experimental fluence ϕ to dose per atom we use

$$\text{Dose/atom} = F_{D_n} \phi V_{\text{atom}},$$

$$V_{\text{atom}} = a^3/8 \text{ atoms in unit cell}, \quad (\text{A6})$$

where a is the lattice constant of Ge and F_{D_n} is the nuclear-deposited energy by the Si ions into the Ge film placed between the SiO₂ layers as obtained from SRIM2008.³⁹

To determine the energy added to the NC in each recoil, we analyze what fraction f_{NC} of the additional potential and kinetic energy brought in by the recoil is distributed between to the NC as compared to the silica matrix. This is done by removing a thermal energy corresponding to the current temperature $1.5k_B T$ from the kinetic energy of each atom $E_{\text{kin},i}$ in the simulation cell. The potential energy of the atoms in the beginning of the recoil simulation E_{pot}^0 is removed from the potential energy E_{pot} to include only the energy added by the recoil. For E_{pot} we used the potential energy stored in the cell after the atomic cascades came to an end, but before the energy had been removed from the cell at the boundaries. At the same time we collected the kinetic energy of atoms E_{kin} . Thus,

$$f_{\text{NC}} = \frac{\Delta E_{\text{tot}}^{\text{NC}}}{\Delta E_{\text{tot}}^{\text{NC+SiO}_2}}. \quad (\text{A7})$$

We calculate the total energy ΔE_{tot} for NC atoms and for the whole cell (including both NC and SiO₂ atoms) as follows:

$$\Delta E_{\text{tot}} = \sum_{i=1}^N (E_{\text{kin},i} - 1.5k_B T + E_{\text{pot},i} - E_{\text{pot},i}^0). \quad (\text{A8})$$

Our calculations show that, for instance, in the case of 1 keV recoil in a 4 nm Ge NC, on an average 30% of the recoil energy goes to the NC atoms and the rest to the matrix. The dose added by each recoil is thus

$$\text{Dose/atom} = f_{\text{NC}} * (E_{\text{rec}} - E_{D_e}), \quad (\text{A9})$$

where the total energy lost to electronic stopping E_{D_e} is

removed to be consistent with the conversion from fluence to dose per atom. However, for comparison with experiments, this conversion can be validly done only for the recoil spectrum simulations. This is because low-energy recoils on the SiO₂ side are highly unlikely to hit the nanocrystal, an effect

which the monoenergetic recoil calculation misses. Hence for direct comparison with experiments, we can only use the recoil spectrum calculations.⁴⁰ The Ge bulk amorphization simulation is not affected by this complication, since in those cases all energies are guaranteed to be lost to Ge.

*flyura.djurabekova@helsinki.fi

- ¹G. Kellermann and A. F. Craievich, *Phys. Rev. B* **65**, 134204 (2002).
- ²G. Kellermann and A. F. Craievich, *Phys. Rev. B* **78**, 054106 (2008).
- ³J. A. Pakarinen, M. Backman, F. Djurabekova, and K. Nordlund, *Phys. Rev. B* **79**, 085426 (2009).
- ⁴D. V. Melnikov and J. R. Chelikowsky, *Phys. Rev. B* **69**, 113305 (2004).
- ⁵C. Garcia, B. Garrido, P. Pellegrino, R. Ferre, J. A. Moreno, J. R. Morante, L. Pavesi, and M. Cazzanelli, *Appl. Phys. Lett.* **82**, 1595 (2003).
- ⁶G. Rizza, H. Cheverry, T. Gacoin, A. Lamas, and S. Henry, *J. Appl. Phys.* **101**, 014321 (2007).
- ⁷Z.-Q. Xie, Z.-H. Li, W.-B. Fan, D. Chen, Y.-Y. Zhao, and M. Lu, *Appl. Surf. Sci.* **253**, 5501 (2007).
- ⁸S. Cheylan, N. Langford, and R. G. Elliman, *Nucl. Instrum. Methods Phys. Res. B* **166-167**, 851 (2000).
- ⁹B. Johannessen, P. Kluth, D. J. Llewellyn, G. J. Foran, D. J. Cookson, and M. C. Ridgway, *Appl. Phys. Lett.* **90**, 073119 (2007).
- ¹⁰D. Pacifici, E. C. Moreira, G. Franzo, V. Martorino, F. Priolo, and F. Iacona, *Phys. Rev. B* **65**, 144109 (2002).
- ¹¹L. L. Araujo, R. Giulian, D. J. Sprouster, C. S. Schnohr, D. J. Llewellyn, P. Kluth, D. J. Cookson, G. J. Foran, and M. C. Ridgway, *Phys. Rev. B* **78**, 094112 (2008).
- ¹²L. L. Araujo, R. Giulian, B. Johannessen, D. J. Llewellyn, and P. Kluth, G. de M. Azevedo, D. J. Cookson, and M. C. Ridgway, *Nucl. Instrum. Methods Phys. Res. B* **266**, 3153 (2008).
- ¹³J. F. Ziegler, J. P. Biersack, and U. Littmark, *The Stopping and Range of Ions in Solids* (Pergamon, New York, 1985).
- ¹⁴J. Hester, AVERAGE computer code, 2007, available online at <http://anbf2.kek.jp/xafs-downloads.html>.
- ¹⁵B. Ravel and M. Newville, *J. Synchrotron Radiat.* **12**, 537 (2005).
- ¹⁶S. D. Kelly and B. Ravel, in *X-Ray Absorption Fine Structure—XAFS13: 13th International Conference*, edited by B. Hedman and P. Pianetta, AIP Conf. Proc. No. 882 (AIP, New York, 2007) p. 132.
- ¹⁷J. J. Rehr and R. C. Albers, *Rev. Mod. Phys.* **72**, 621 (2000).
- ¹⁸M. Newville, *J. Synchrotron Radiat.* **8**, 322 (2001).
- ¹⁹L. L. Araujo, P. Kluth, G. de M. Azevedo, and M. C. Ridgway, *Phys. Rev. B* **74**, 184102 (2006).
- ²⁰S. von Alfthan, A. Kuronen, and K. Kaski, *Phys. Rev. B* **68**, 073203 (2003).
- ²¹K. Nordlund, 2006, PARCAS computer code. The main principles of the molecular-dynamics algorithms are presented in Refs. [25](#) and [41](#). The adaptive time step and electronic stopping algorithms are the same as in Ref. [30](#).
- ²²T. Watanabe, D. Yamasaki, K. Tatsumura, and I. Ohdomari, *Appl. Surf. Sci.* **234**, 207 (2004).
- ²³J. Samela, K. Nordlund, V. N. Popok, and E. E. B. Campbell, *Phys. Rev. B* **77**, 075309 (2008).
- ²⁴K. Ding and H. C. Andersen, *Phys. Rev. B* **34**, 6987 (1986).
- ²⁵K. Nordlund, M. Ghaly, R. S. Averbach, M. Caturla, T. Diaz de la Rubia, and J. Tarus, *Phys. Rev. B* **57**, 7556 (1998).
- ²⁶D. R. Lide, *CRC Handbook of Chemistry and Physics*, 82nd ed. (CRC Press, Boca Raton, USA, 2001).
- ²⁷L. Giacomazzi and A. Pasquarello, *J. Phys.: Condens. Matter* **19**, 415112 (2007).
- ²⁸F. Djurabekova and K. Nordlund, *Phys. Rev. B* **77**, 115325 (2008).
- ²⁹G. C. Rizza, M. Strobel, K. H. Heinig, and H. Bernas, *Nucl. Instrum. Methods Phys. Res. B* **178**, 78 (2001).
- ³⁰K. Nordlund, *Comput. Mater. Sci.* **3**, 448 (1995).
- ³¹A presentation of the MDRANGE computer code is available on the World Wide Web in http://beam.acclab.helsinki.fi/~knordlun/mdh/mdh_program.html.
- ³²F. Djurabekova, M. Backman, and K. Nordlund, *Nucl. Instrum. Methods Phys. Res. B* **266**, 2683 (2008).
- ³³K. Nordlund and R. S. Averbach, *Phys. Rev. B* **56**, 2421 (1997).
- ³⁴D. Bazin and J. J. Rehr, *J. Phys. Chem. B* **107**, 12398 (2003).
- ³⁵G. Dalba and R. Grisenti, *J. Non-Cryst. Solids* **338-340**, 201 (2004).
- ³⁶L. L. Araujo, G. J. Foran, and M. C. Ridgway, *J. Phys.: Condens. Matter* **20**, 165210 (2008).
- ³⁷M. Vaccari and P. Fornasini, *J. Synchrotron Radiat.* **13**, 321 (2006).
- ³⁸I. Jenčič, M. W. Bench, I. M. Robertson, and M. A. Kirk, *J. Appl. Phys.* **78**, 974 (1995).
- ³⁹J. F. Ziegler, SRIM2008 software package, available online at <http://www.srim.org>.
- ⁴⁰In a preliminary presentation of some aspects of this work, we presented a direct comparison of the monoenergetic recoils to experiments (Ref. [42](#)). However, that comparison did not take into account the issue with low-energy recoils, and thus is misleading.
- ⁴¹M. Ghaly, K. Nordlund, and R. S. Averbach, *Philos. Mag. A* **79**, 795 (1999).
- ⁴²F. Djurabekova, M. Backman, O. H. Pakarinen, K. Nordlund, L. Araujo, and M. Ridgway, *Nucl. Instrum. Methods Phys. Res. B* **267**, 1235 (2009).